Non-destructive evaluation of the steel fibre content and anisometry in thin UHPFRC elements
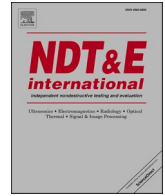
Pimentel, Mário; Sine, Aurélio; Nunes, Sandra

Important note
To cite this publication, please use the final published version (if applicable).
Please check the document version above.

Non-destructive evaluation of the steel fibre content and anisometry in thin UHPFRC elements

Mário Pimentel [a,*], Aurélio Sine [b], Sandra Nunes [c]

[a] CONSTRUCT-LABEST, Faculty of Engineering (FEUP), University of Porto, Portugal
[b] Laboratory of Engineering of Mozambique (LEM), Mozambique
[c] Delft University of Technology (TU Delft), Delft, the Netherlands

ABSTRACT

The tensile response of ultra-high performance fibre-reinforced composites (UHPFRC) is decisive in many applications and depends on the steel fibre content and orientation. These vary troughout the structural element and may differ from those in the laboratory specimens used to characterize the material behaviour. This work presents the developments on a non-destructive test method based on the measurement of the magnetic inductance, substantiating its use for the determination of the fibre content and orientation in thin UHPFRC elements and allowing the estimation of the directionally dependent post-cracking tensile strength of the material in the structure. Starting from a probabilistic description of the fibre orientation, an existing physical model of the magnetic circuit composed of a U-shaped inductor and the composite is generalized and is used to derive the relations between the magnetic inductance measurements, the fibre volumetric fraction and the fibre orientation factor. A second-order tensor approximation of the relative magnetic permeability of the composite is proposed to determine the in-plane fibre orientation factor along any direction based on any three non-collinear measurements. Experimental evidence is presented supporting the theoretical developments. The factors that may affect the measurements are experimentally quantified. The paper concludes with an application example.

1. Introduction

Ultra-high performance fibre-reinforced cementitious composites (UHPFRC) is the adopted designation for a family of composite materials, also designated as reactive powder concretes [1], constituted by a compact cementitious matrix embedding a large number of short steel fibres [2,3]. The high mechanical resistance and the high unit cost of the material make it suitable for materializing thin structural elements, such as slender bridge deck slabs or beams with thin webs (Fig. 1). UHPFRC can be prestressed or reinforced with ordinary steel bars. In many structural concepts, the prestress strands (or the reinforcement bars) are placed on longitudinal and/or transversal ribs, delimiting thin (40–60 mm thick) panels of unreinforced UHPFRC. The strengthening and rehabilitation of existing reinforced concrete (RC) structures through application of thin (generally 30–60 mm thick) layers of UHPFRC [4–6] constitutes another relevant field of application, see also Fig. 1.

The tensile response of the UHPFRC schematically represented in Fig. 2 is critical for the performance of the thin unreinforced UHPFRC elements. The composite remains crack-free until the limit of elasticity in tension (f_{Ute}) is reached. In the case of short-fibre polymeric composites [7–9], the elastic properties – Young modulus and limit of elasticity in tension – depend on the anisometric fibre structure. In the case of UHPFRC, it is shown in Ref. [10] that this dependence can also be observed for f_{Ute}. In the inelastic regime, depending on the fibre type, content and orientation [11–15], a strain hardening phase may be achieved, characterized by the formation of a stable microcrack pattern. When the post-cracking tensile strength (f_{Utu}) is reached, the deformations localize in a macrocrack that can still carry significant residual tensile stresses until the full stress release. This behaviour is thoroughly discussed in Refs. [16,17]. The post-cracking tensile strength along the *i*-direction, $f_{Utu,i}$, can be determined using the equation first proposed by Naaman [18,19]:

$$f_{Utu,i} = \tau_f \; \alpha_{0,i} \; \alpha_{1,i} V_f \; \frac{l_f}{d_f} = \tau_f \cdot \lambda_i \tag{1}$$

where τ_f is a representative value of the fibre-to-matrix bond, $\alpha_{0,i}$ and $\alpha_{1,i}$ are the fibre orientation and efficiency factors, respectively, V_f is the
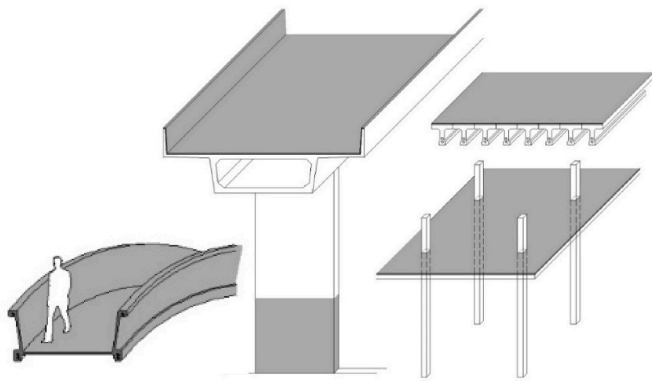
Fig. 1. Structural applications of UHPFRC involving thin (30–60 mm) UHPFRC elements or layers.
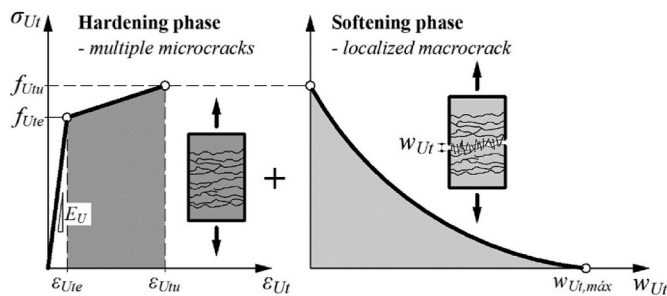

Fig. 2. UHPFRC constitutive law with hardening under uniaxial tension.

volumetric fibre fraction, l_f and d_f, the length and diameter of the fibres. The fibre parameters related to orientation, efficiency, content and geometry can be lumped on the directionally dependent fibre structure parameter, λ_i. This equation was validated for UHPFRC with varying fibre content and orientation profiles [13,17,20].

The tensile constitutive law of UHPFRC can be directly obtained from the uniaxial (direct) tensile test (UTT) [13,21,22], or from the four-point bending test (FPBT) using inverse analysis [23–29]. The double-edge wedge-splitting test (DEWST) has also been shown to be a suitable test for the direct determination of the post-cracking tensile strength f_{Utu} [30–32]. However, the distribution of the fibres in a UHPFRC element depends on the rheology of the composite in the fresh state and the casting procedure [16,33–39]. Usually, self-compacting mixtures are considered, potentially leading to flow-induced fibre orientation [40–42] and to the anisotropic tensile behaviour of the material [43–46]. The latter is the direct consequence of anisometric fibre distribution that can be described using stereological principles and geometric probability theory [12,46–48]. It is also known that mixes with excessive fluidity may lead to fibre sedimentation across the thickness of horizontally cast elements or towards the base of vertically cast panels. Moreover, uneven fibre distribution may occur whenever two casting fronts meet, creating a weak discontinuity in the element which may govern the behaviour [49–52]. All this makes the tensile response of the material in the structure to differ from that obtained with laboratory specimens. The use of test specimens cut from larger panels provides one way to assess these effects [14,38,52–54], but is both costly and time-consuming.

Suitable quality control methods providing reliable indicators of the "in-structure" fibre content and orientation are necessary to ensure the envisaged structural performance is achieved. Non-destructive test (NDT) methods pursuing this objective have been developed based on measurements of the electric resistivity [55–58], AC-impedance spectroscopy (AC-CS) [59] and magnetic properties of the fibres [51,60–65]. In particular, the NDT methods based on the magnetic inductance

measurements provided by U-shaped probes placed over the surface of thin UFPFRC elements have shown great potential for field applications [51,60,61,65].

2. Research objectives and significance

This work presents further developments on the NDT method proposed by Nunes et al. [20,65], recently adopted by other researchers [54,66,67,10] and recommended in the new swiss code for UHPFRC structures [68] currently under consultation. These developments are decisive for substantiating its use in the determination of the fibre content and orientation indicators in thin UHPFRC elements and allow the estimation of the directionally dependent "in structure" post-cracking tensile strength along any direction of interest based on any three non-collinear measurements.

3. Description of the fibre orientation

In the three-dimensional space (3D), a fibre can freely rotate according to the angles θ (polar) and φ (azimuthal), and all possible orientations describe the surface of a sphere (Fig. 3(a)). On the other hand, in the two-dimensional case (2D), the fibres are considered to lie on parallel planes, all possible orientations of a fibre describe a circumference (Fig. 3(b)) and are defined by the angle, θ. However, depending on the element thickness and the fibre position relative to its depth, the fibre rotation can be limited. For this reason, the fibre distribution on real thin elements is not exactly represented by a 2D nor by a 3D distribution [69,70]. In fact, it can be taken as a 3D distribution with truncated limits expressing the so-called "wall effects".

According to French norm NF P18-710 [71], UHPFRC thin elements are considered those with a thickness not greater than three times the length of fibres, $h_U/l_f \leq 3$ (where l_f is the length of the longest fibres contributing to ensuring non-brittleness). In this work, it is considered that thin elements are those where the fibre orientation distribution varies essentially in xy-plane, perpendicular to the element thickness (Fig. 4). In particular, it is assumed that the direction of preferential fibre orientation is parallel to the xy plane.

3.1. Probability density function

The fibre orientation state in 3D or 2D can be described using the probability density function, $\psi(\theta,\varphi)$. Some assumptions have to be taken into account: the fibres are rigid cylinders, uniform in length and diameter, and are uniformly distributed in space (3D) or in the plane (2D) [72]. The orientation of a fibre can be described using a spherical coordinate system in 3D (Fig. 3(a)) or in a polar coordinate system in 2D (Fig. 3(b)).

Since a fibre oriented at any angles (θ,φ) is indistinguishable from another oriented at $(\pi-\theta, \varphi+\pi)$, the probability density function of the fibre orientation, $\psi(\theta,\varphi)$ is π-periodic. To account for this property,

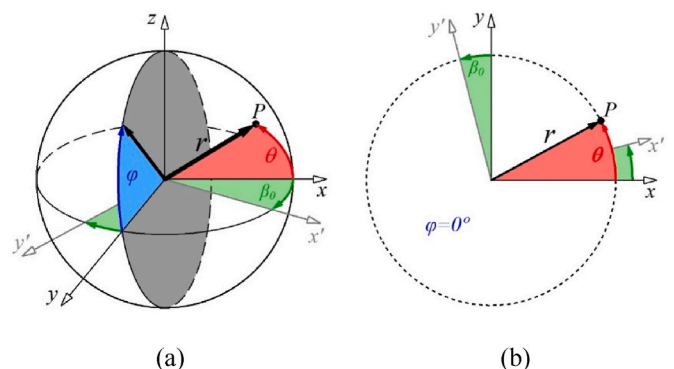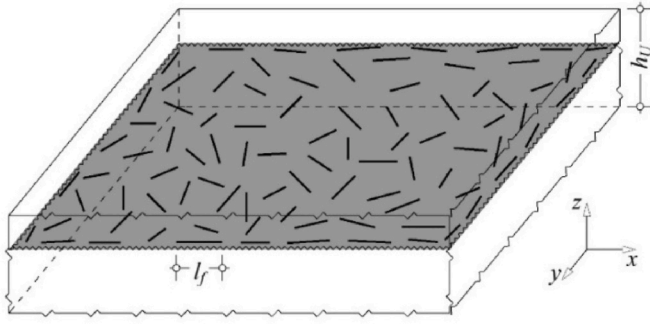**Fig. 3.** Representation of fibre orientation in (a) 3D and (b) 2D.

Fig. 4. Fibre distribution in the *xy*-plane.

Guenet [73] used the following bell-shaped function:

$$\Psi(\theta, \varphi) = \cosh\left(k_g \cos\theta\right) \tag{2}$$

where $k_g \geq 0$ is a parameter that characterizes the sharpness of the function: $k_g = 0$ defines a uniform distribution, and when $k_g \to \infty$, Ψ tends to Dirac Delta function, i.e., the orientation becomes unidirectional (1D). Eq. (2) is expressed in such a way that the default preferential orientation of the fibres (maximum value of Ψ) is along the *x*-axis. By rotating the *xy*-plane around the *z*-axis, the preferential in-plane orientation becomes defined by the angle β_0 (see Fig. 3). After some mathematical manipulation it can be shown that the final probability density functions of the fibre orientation in the 3D and 2D cases are given in Eq. (3) (a) and (b), respectively:

$$3D : \psi(\theta, \varphi) = \frac{k_g}{2\pi \sin h k_g} \cosh\left[k_g(\cos\theta\cos\beta_0 + \sin\theta\cos\varphi\sin\beta_0)\right] (a) \tag{3}$$

$$2D : \psi(\theta) = \frac{\cosh\left[k_g(\cos\theta\cos\beta_0 + \sin\theta\sin\beta_0)\right]}{\int_{\theta=0}^{\pi} \cosh\left[k_g(\cos\theta\cos\beta_0 + \sin\theta\sin\beta_0)\right] d\theta} (b)$$

The derivation of Eq. (3) is presented in Appendix A of the suplementary material. By applying Eq. (3) (b), considering $k_g = 0, 2, 10$ and the preferential in-plane orientation of the fibres $\beta_0 = 30°$, the graphic representations of the 2D-probability density functions are presented in Fig. 5. The corresponding representation for the 3D case in the spherical coordinate system is provided in Appendix A.

3.2. Scalar descriptors

Simpler descriptions of the fibre orientation are obtained using scalar variables. For the readers not familiar with these concepts, reference is made to Appendix B. In particular, the fibre orientation factor, $\alpha_{0,i}$, defined as the probability of a single fibre to intersect a random planar

surface normal to a given *i*-axis is of particular interest. This scalar is used as an input variable in engineering models for determining the anisotropic post-cracking tensile strength, $f_{Utu,i}$, as per Eq. (1), or the fibre efficiency factor, $\alpha_{1,i}$, as per Eq. B. (7).

The procedures for quantifying $\alpha_{0,i}$ in thin elements in which the boundaries constrain the orientation of the fibres (wall effects) are described the Appendix C.

4. Non-destructive test method

4.1. Fundamentals

The magnetic permeability of a material, μ, can be defined as the constant of proportionality between the magnetizing field strength to which the material is subjected and the resultant magnetic flux density inside the material. In isotropic mediums, μ is a scalar, becoming a second order tensor in anisotropic mediums. It can be more conveniently expressed in terms of relative magnetic permeability μ_r, which is the factor by which the material permeability exceeds that of free space, μ_0, that is: $\mu_r = \mu/\mu_0$. UHPFRC is a composite constituted by two phases: the matrix, with a relative magnetic permeability $\mu_{rm} = 1.0$, similar to that of the air and independent of the mix composition and age; and the fibres, which show ferromagnetic behaviour, i. e, $\mu_{rf} \gg 1$. This makes the measurement of any physical quantity depending on the magnetic permeability of the composite a good candidate for providing information on both the amount and orientation of the fibres.

In a previous work by Nunes et al. [65], an inductor was developed consisting of a U-shaped ferrite core with a copper wire coil wound round both legs (see Fig. 6). A magnetic field is generated when an electric current passes through the copper winding. The inductance, *L*, is the ratio of the magnetic flux to current and can be measured using an LCR meter, as depicted in Fig. 6 (b). If the U-shaped inductor is placed over a UHPFRC layer, the inductance of the resulting magnetic circuit depends on the relative magnetic permeability of the composite according to the equation derived in Ref. [65]:

$$L_i = \frac{N^2 \mu_0}{\frac{l_c/A_c}{\mu_{rc}} + \frac{l/A}{\mu_{r,i}}} \tag{4}$$

where the subscript $(.)_i$ refers to any in-plane direction along which the inductance is being measured, *N* is the number of turns in the coil; l_c/A_c is ratio between the length of the magnetic path through the U-shaped core and its cross-sectional area; μ_{rc} is the relative magnetic permeability of the core material (ferrite); and $\mu_{r,i}$ is the relative magnetic permeability of the composite along the *i*-direction. The ratio l/A relates to geometrical properties of the magnetic field path through the composite layer. Knowing that μ_{rc} and $\mu_{r,i}$ differ by three orders of magnitude, and
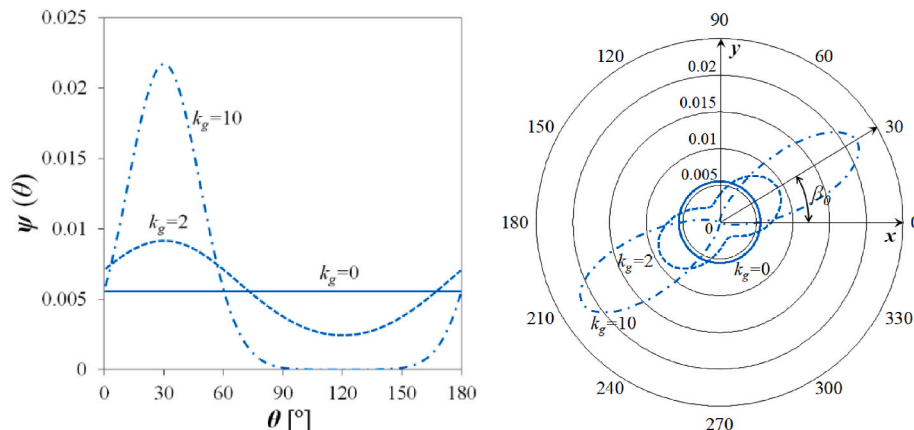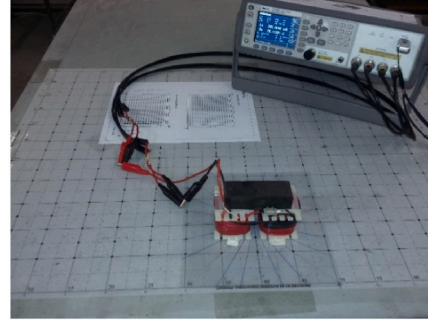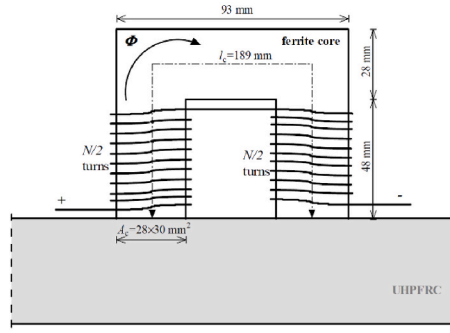

Fig. 5. 2D-Probability density functions: (a) ψ as a function of the polar coordinate θ; (b) representation on the polar coordinate system.

Fig. 6. NDT method (a) schematic representation of the magnetic circuit constituted by probe and UHPFRC layer [65]; and (b) measurements on a UHPFRC thin element.

assuming that the ratio l/A remains approximately unchanged when the inductance L_{air} is measured placing the probe in the air, away from any magnetic object, the relative magnetic permeability of the composite can be estimated experimentally according to:

$$\mu_{r,i} \approx \frac{L_i}{L_{air}} \qquad (5)$$

4.2. Simplified physical model of the composite

A simple model of the composite supporting the NDT method was developed in Ref. [65]. As previously mentioned, the composite is considered as a two phase material, matrix and fibres, with relative magnetic permeability equal to $\mu_{rm} = 1.0$ and $\mu_{rf} > 1$, respectively. Negligible interaction is assumed between the fibres. The fibres are assumed to lie on parallel planes and to be aligned in the same direction, that is, the orientation is 2D and is described by a Dirac delta function. This model is herein generalized. Instead of a Dirac delta, the 2D probability density function given by Eq. (3) (b) is adopted instead, allowing for more realistic in-plane distribution of fibres in thin UHPFRC elements.

The orientation angle of the probe (alignment of the legs) is defined by the angle β and the orientation angle of the fibres is defined by θ, both measured with respect to the x-axis, according to Fig. 7. Let $dV_{fn} = \psi(\theta_n) V_f d\theta$ be the infinitesimal volumetric fraction of fibres oriented between θ_n and $(\theta_n + d\theta)$. Likewise in Ref. [65], the fibre volume is divided in two parts. However, in this generalized model this division is made for each infinitesimal group of fibres, such that $dV_{fn} = dV_{f,n,//} + dV_{f,n,\perp}$
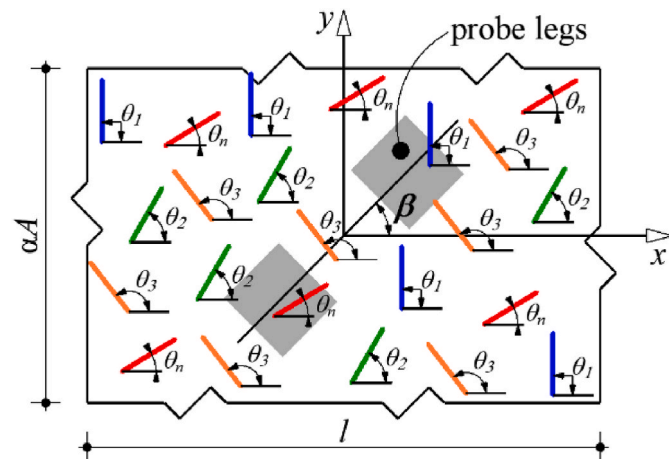
- $dV_{f,n,//} = dV_{f,n} \cdot \cos^2(\beta - \theta_n)$ corresponds to the part $dV_{f,n}$ parallel to the measuring direction;
- $dV_{f,n,\perp} = dV_{f,n} \cdot \sin^2(\beta - \theta_n)$ corresponds to the part $dV_{f,n}$ perpendicular to the measuring direction;

The relative magnetic permeability of a thin UHPFRC element for any alignment β of the probe can be calculated according to the in-plane generalized simplified physical model as follows (see Ref. [65] for further details):

$$\mu_{r,\beta} = \left\{ \frac{(1-\gamma)V_{f,\perp}}{\gamma + \mu_{rf} \cdot (1-\gamma)} + \frac{\left[1-(1-\gamma)V_{f,\perp}\right] \cdot \left(\mu_{rf} \cdot \gamma + 1-\gamma\right)}{\left[1-(1-\gamma)V_{f,\parallel}\right] \cdot \left(\mu_{rf} \cdot \gamma + 1-\gamma\right) + \mu_{rf} \cdot (1-\gamma)V_{f,\parallel}} \right\}^{-1} \qquad (6)$$

where γ is a model parameter expressing the fact that the fibres are discontinuous steel filaments. In this generalized model, the volume projections are given by $V_{f,\parallel} = V_f \int \psi(\theta) \cos^2(\beta-\theta) d\theta$ and $V_{f,\perp} = V_f \int \psi(\theta) \sin^2(\beta-\theta) d\theta$.

Polar representations of the relative magnetic permeability are shown in Fig. 8, considering the probability density functions defined by $k_g = 2$ and 5 and $\beta_0 = 30°$. The alignment of the maximum relative magnetic permeability and preferential fibre orientation directions is evident. It is also noticed that the model predicts the average of the relative magnetic permeability ($\mu_{r,mean}$) along any two orthogonal directions β and $\beta+\pi/2$ to be constant and independent of k_g, that is, independent of the fibre orientation profile.

4.3. Approximation via a 2nd order tensor

The relative magnetic permeability given of the theoretical model can be approximated by a 2nd order tensor. Thus, the relative magnetic permeability for any alignment defined by the angle β, $\mu_{r,\beta}$, can be retrieved from the relative magnetic permeability along any three non-collinear directions. In particular, knowing $\mu_{r,i}$, $\mu_{r,j}$ and $\mu_{r,i+\pi/4}$ (see Fig. 9), $\mu_{r,\beta}$ can be determined using Eq. (7):

$$\mu_{r,\beta} = \mu_{r,i} \cdot \cos^2\beta + \mu_{r,j} \cdot \sin^2\beta + \left[\mu_{r,i+\pi/4} - \mu_{r,mean}\right]\sin 2\beta \qquad (7)$$

where $\mu_{r,mean}$ is the mean relative magnetic permeability between the two orthogonal directions, i and j.

The directions of maximum and minimum magnetic permeability can also be determined using the usual tensor operations. These provide the visualization of the directions of the preferential fibre orientation in larger specimens where inductance measurements are performed in a grid of points. This will be exemplified in section 6.2.

4.3.1. Validation

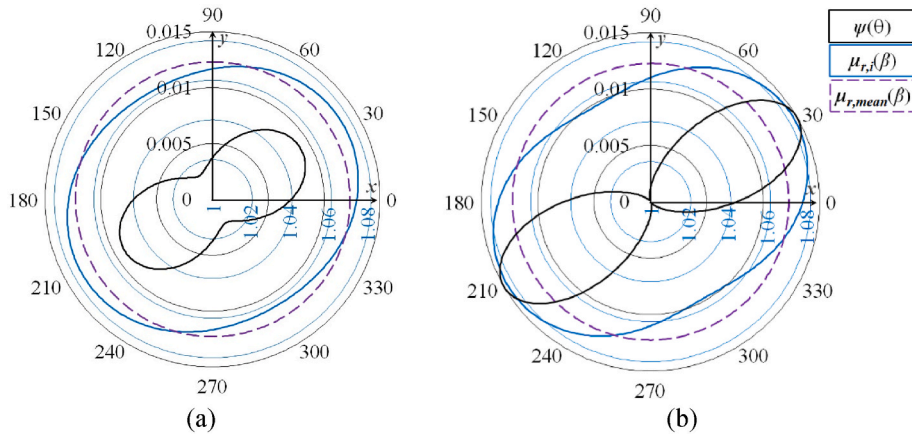A NDT campaign was conducted in 24 DEWST specimens with 150 ×

Fig. 7. Definition of in-plane orientation angles of fibres.

Fig. 8. Polar representation of relative magnetic permeability for $\beta_0 = 30°$ and (a) $k_g = 2$ and (b) $k_g = 5$.
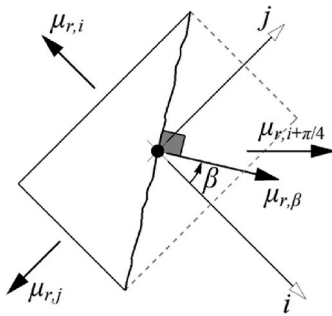

Fig. 9. 2nd order tensor approximation of the relative magnetic permeability.

$150 \times 30\,\text{mm}^3$, containing fibre volumetric fractions of 1, 2, 3 and 4 % of fibres with $l_f/d_f = 13/0.2$ (mm/mm) and three fibre orientation profiles: oriented ($\beta_0 = 0°$ and 90°) and not-oriented. As depicted in Fig. 10(a), each mould has the dimensions $304 \times 150 \times 30\,\text{mm}^3$ and is cut along the centreline to produce two similar DEWST specimens. A single batch is used to fill each mould so as to guarantee the nominal fibre content. Following the procedure and the setup detailed in Refs. [20,65], the orientation of the fibres is achieved by casting specimens within a magnetic field capable of orienting the fibres while the material is in the fresh state. The specimens without preferential fibre orientation were cast by placing the material in the centre and allowing it to flow until the mould is filled.

The inductance measurements L_i were taken over the moulded face every 15° (see Fig. 10(b)) and the relative magnetic permeability determined according to Eq. (5). The dots in Fig. 11 represent the average of the measurements taken on the two similar specimens in each mould and the lines provide the tensor approximation according to Eq. (6). The agreement is noticeable. In the specimens with no preferential orientation of the fibres, the polar representation of the relative magnetic permeability shows a figure with nearly constant radius. In the specimens with preferential fibre orientation along $\beta_0 = 0°$ or 90° the radius variation is clearly variable, being maximum at $\beta = \beta_0$ and minimum in the perpendicular direction.

4.4. Determination of the fibre content

As shown in section 4.2, the model predicts that the mean relative magnetic permeability along two orthogonal directions and given by Eq. (8) is nearly insensitive to the fibre orientation distribution and may serve as an indicator of the fibre content.

$$\mu_{r,mean} = \frac{1}{2}\left(\mu_{r,i} + \mu_{r,j}\right) \tag{8}$$

Additionally, is has been proposed in Ref. [65] that ($\mu_{r,mean} - 1$) increases linearly with the fibre volumetric fraction:

$$V_f = \frac{\mu_{r,mean} - 1}{k_v} \tag{9}$$

where k_v is the proportionally constant and depends on the geometric and magnetic permeability of the fibres. This can be accounted for in the model through the parameters γ and μ_{rf}. Fig. 12 shows the model predictions considering a fibre distribution with $k_g = 5$ and $\beta_0 = 0°$, and the
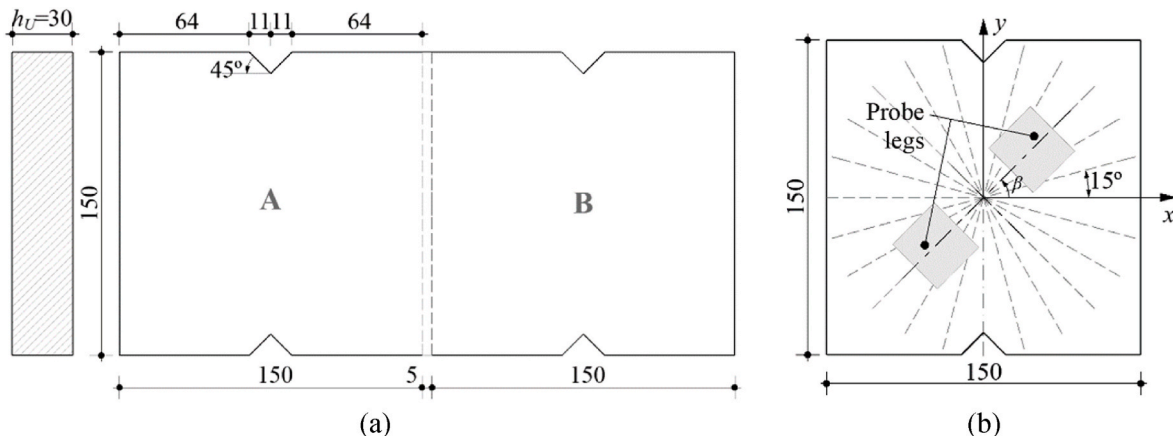

Fig. 10. DEWST specimens: (a) Dimensions (mm) of the mould for two identical specimens; (b) scheme of the probe measurement and notation.
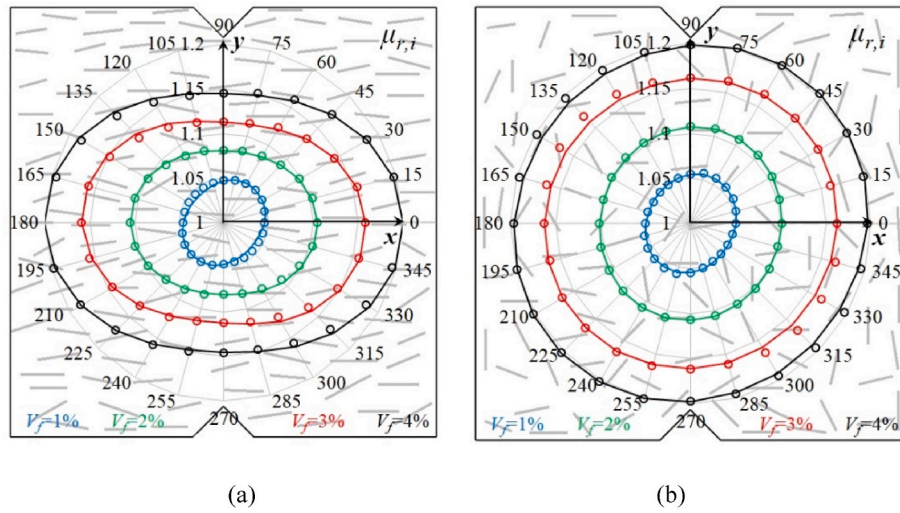
Fig. 11. Polar representation of the relative magnetic permeability of DESWT2 plates (a) fibres preferentially oriented at $\beta_0 = 0°$ and (b) fibres without preferential orientation.
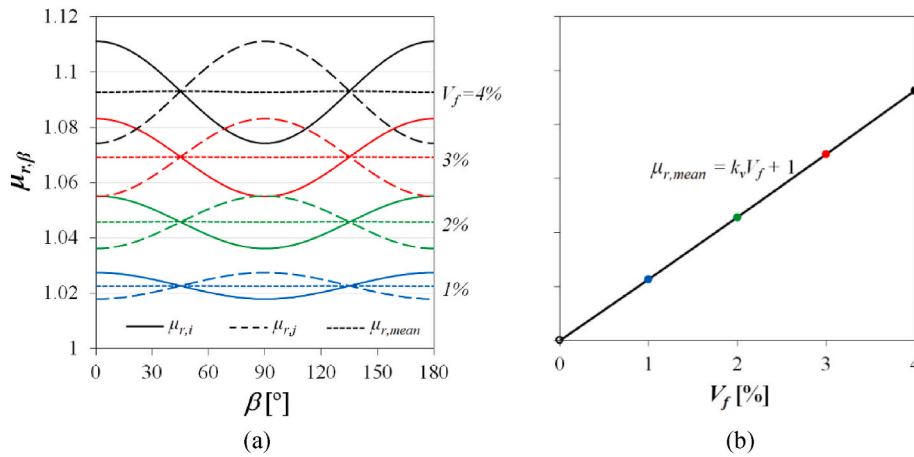

Fig. 12. Model predictions: (a) Relative magnetic permeability variation with V_f and β;(b) relation between V_f and $u_{r,mean}$.

parameters $\gamma = 0.37$ and $\mu_{rf} = 2000$, confirming Eq. (9). As will be discussed in section 5, other factors have a direct influence on k_v which cannot be described by this simple model, such as the element thickness, the finishing of the surface, the fibre sedimentation across the thickness and the distance of the probe to the border of the element.

4.4.1. Validation

The experimental validation of Eq. (9) is made with data from three experimental campaigns, totalizing 58 specimens and varying the fibre volumetric fraction, the fibre orientation profiles, the fibre geometry and the element thickness. The experimental data is summarized in Table 1. The measurements were made on the moulded face of DEWST specimens with the same in-plane dimensions $150 \times 150mm^2$. The specimens of the series DEWST1 and DEWST3 are those of reference [65], and the DEWST2 are those mentioned in section 4.3.1. In Table 1 is also shown the k_v providing the best fit to the data of each experimental series. As expected, k_v increases with the length of the fibres. This shows that if the fibre volumetric fraction is to be determined in a given structural element, previous calibration of the slope k_v of the regression line must be performed in the laboratory in specimens with known fibre content and the same type of fibres. The results are independent of the cementitious matrix.

The results are shown in Fig. 13. It can be seen that Eq. (9) is within the 90 % confidence lines of the linear regression model, further

Table 1
Specimens used to validate Eq. (9).

Ref.	h_U	l_f	d_f	V_f	Fibre orientation			k_v
					x	[−]	Not-orient.	
	[mm]	[mm]	[mm]	[%]				
DEWST1	25	9-12[a])	0.175	0.5	2	2	2	4.12
				1.5	2	2	2	
				3.0	2	2	2[b])	
DEWST2	30	13	0.2	1.0	2	2	2	4.68
				2.0	2	2	2	
				3.0	2	2	2	
				4.0	2	2	2	
DEWST3	25	10	0.175	1.0	2	–	2	3.90
				2.0	2	–	2	
				3.0	2	–	2	
				4.0	2	–	2	

[a] 50 % of each.

[b] $\mu_{r,mean}$ measurements on these specimens were identified in Ref. [65] as outliers and are not considered here for the determination of k_v indicated in the table.

confirming its validity. A finer analysis indicates that the scatter in the series DEWST1 and DEWST3 increases noticeably above $V_f = 3$ %. The most likely explanation relies on the fact that the inductance measurements are quite sensitive to the uneven distribution of the fibres across
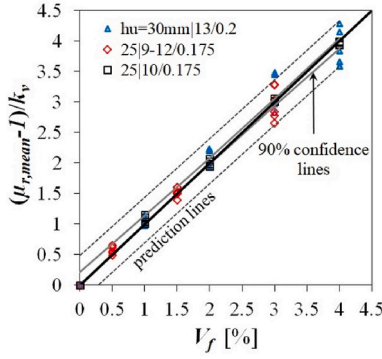
Fig. 13. Normalized fibre content indicator versus the volumetric fibre fraction.

the thickness of the specimens, most often due to fibre sedimentation. This will be discussed in detail in section 5.3. It is recalled that the measurements were performed over the moulded (bottom) face and it cannot be ruled out that in some specimens this may have contributed to at least part of the observed scatter.

4.5. Determination of the fibre orientation factor

The fibre orientation indicator, ρ_{ij}, given by:

$$\rho_{ij} = \frac{\mu_{r,i} - \mu_{r,j}}{2(\mu_{r,mean} - 1)} \qquad (10)$$

was introduced in Ref. [65] as being practically independent of the fibre content. Positive values of ρ_{ij} indicate orientation of the fibres along the *i*-direction, and along *j*-direction, otherwise. Values close to zero indicate no preferential orientation. Later, Nunes et al. [20] identified experimentally a linear relation between ρ_{ij} and the fibre orientation factor, $\alpha_{0,i}$, allowing its determination from the NDT measurements. This is here further explored using the model introduced in section 4.2. In Fig. 14 the theoretical results concerning relation between $\alpha_{0,i}$ and ρ_{ij} are presented using the 2D-probability density function. Different orientation profiles were obtained varying the parameter k_g and inserted in Eq. (6) using the model parameters $\gamma = 0.37$ and $\mu_{rf} = 2000$ to calculate the corresponding relative magnetic permeability $\mu_{r,\beta}$. The angle β was varied between 0° and 90° to obtain the full range of possible ρ_{ij} values for each fibre orientation profile. The corresponding values of $\alpha_{0,i}$ were determined according to Eq. (5) (b). It can be seen that the relation
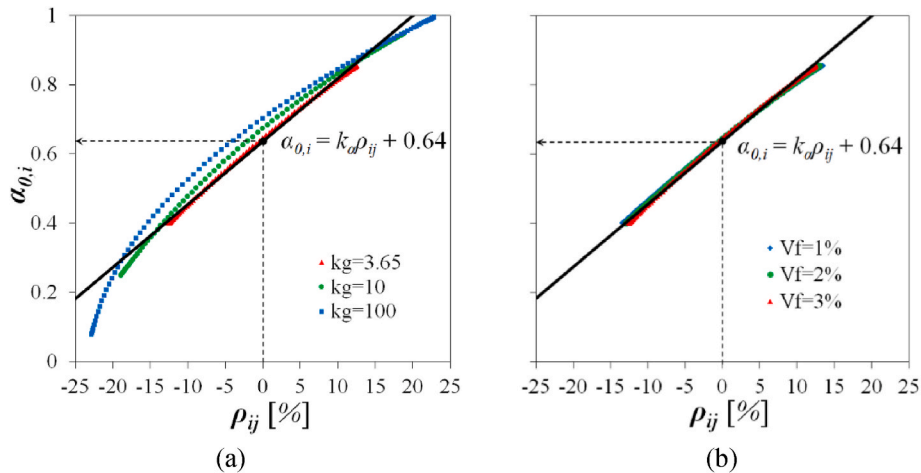
between $\alpha_{0,i}$ and ρ_{ij} becomes closer to linear as k_g approaches values representative of fibre orientation profiles that can be found in practice, for which $k_g = 10$ can be considered as an upper bound. It is noticed that the slope of linear fit to the modelled nonlinear relation remains practically unchanged with varying k_g value.

For a 2D uniform distribution of fibre orientation ($k_g = 0$) we get $\rho_{ij} = 0$ and $\alpha_0 = 0.64$. For elements with finite thickness, it is shown in section B.2 and C of the supplementary material that α_0 is a function of h_U/l_f. Therefore, the general form linear relation is:

$$\alpha_{0,i} = k_\alpha \rho_{ij} + \alpha_0(h_U / l_f) \qquad (11)$$

with k_α being the slope of the linear regression and $\alpha_0(h_U/l_f)$ determined according to Table C1 of the supplementary material.

In Fig. 14(b) it is shown that the influence of fibre volumetric fraction can be neglected for practical purposes.
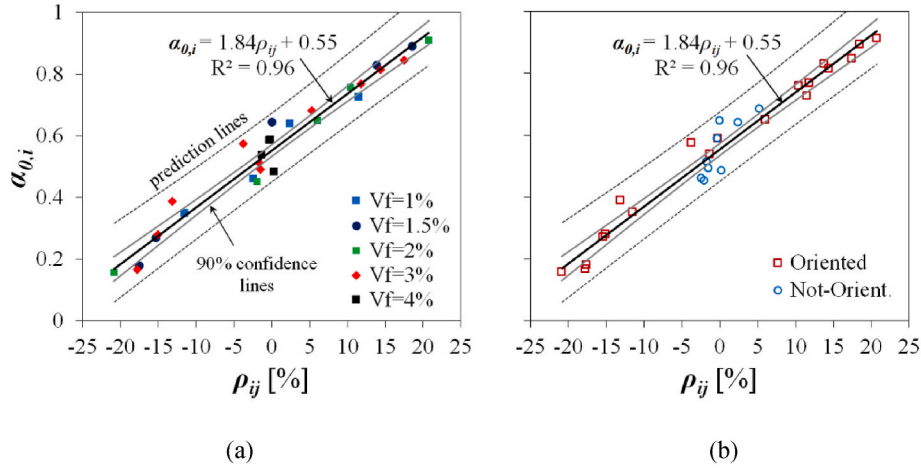
4.5.1. Validation

The validation of the linear relation expressed by Eq. (10), as well as the determination of the slope k_α, is made using the methodology adopted in Nunes et al. [20]. After the mechanical testing of the DEWST specimens over which the NDT measurements reported in section 4.3.1 were made, a cubic sample of $30 \times 30 \times 30 \text{mm}^3$ was cut in the central part of selected specimens, at a distance greater than $l_f/2$ from the crack section to ensure that no fibres were pulled out from the sample. These samples were then used for the determination of $\alpha_{0,i}$ according to Eq. B. (1) given in the supplementary material, following the image analysis procedures described in detail in Ref. [20]. The corresponding values are tabulated in the supplementary material and shown in Fig. 15, jointly with the linear regression line and its 90 % confidence band.

The data covers a wide range of ρ_{ij} and $\alpha_{0,i}$ values and confirms the adequacy of the linear model. As shown in Fig. 15 (a), no discernible effect of fibre volumetric fraction can be detected. All this is in agreement with the trends predicted by the theoretical model. In Fig. 15 (b) the data is labelled according to the orientation profile. The non-oriented specimens present smaller ρ_{ij} values and populate the central part of the regression. The two data points corresponding to oriented specimens located in this central region correspond samples cut at 45° from direction of preferential fibre orientation.

The slope of the regression line indicates that $k_\alpha = 1.84$ with a narrow 90 % confidence band. The intersection at the origin is $\alpha_0 = 0.55$, quite close to the values that can be calculated using the methodology described in section B.2 of the supplementary material considering uniform fibre orientation distribution in elements with finite thickness. In fact, noting that for the ratios $h_U/l_f = 2.1$ for DEWST1 and 2.3 for DEWST2, $\alpha_0 = 0.546$ and 0.542 can be obtained from Table C1 of the

Fig. 14. Theoretical results for the relation between fibre orientation factor and fibre orientation indicator with variation of (a) k_g and (b) V_f.

Fig. 15. Relation between fibre orientation factor and fibre orientation indicator. Specimens labelled according to the: (a) fibre volumetric fraction, V_f; (b) orientation profile.

supplementary material.

The linearization of the relation between ρ_{ij} and $\alpha_{0,i}$ and the fact that, by definition, $\rho_{ij} = -\rho_{ji}$ implies that:

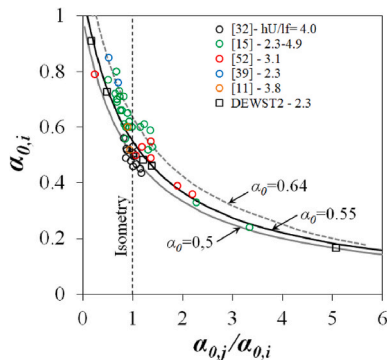$$\alpha_{0,i} = \frac{2\,\alpha_0}{1 + \alpha_{0,j}/\alpha_{0,i}} \tag{12}$$

This equation is independent of the slope k_α and is plotted in Fig. 16 jointly with the experimental data already included in Figure B2 of the supplementary material. It is seen that the equation fits the data at least as well as the more complex Eq. B. (2) and provides further indication of the adequacy of the linearized model relating ρ_{ij} and $\alpha_{0,i}$.

5. Factors influencing the inductance measurements

The simplified model of the magnetic circuit is unable to account the influence of some factors on the inductance measurements, such as the thickness of the element, the area surrounding the measuring point, the segregation of the fibres and the roughness of the surface. An extensive experimental campaign dedicated to investigate these effects is described in referece [74]. In the following sections, the main conclusions are summarized.

5.1. Element thickness

The magnetic field developing through the UHPFRC element depends on its thickness, and so the inductance measurements. In thicker elements more ferromagnetic material is intersected and higher values of the inductance are expected. This has a direct impact on the

calibration of the regression line relating V_f and $\mu_{r,mean}$. To study this effect, four 150 mm diameter and 100 mm tall cylinders were cast, with steel fibre volume fractions of 1 %, 2 %, 3 % and 4 %. The inductance measurements on these cylinders were always performed at the centre of the top surface. The thickness effect was evaluated by successively slicing the cylinder from the base, thus decreasing its height from $h_U = 100$ mm down to $h_U = 20$ mm. For further details on the experimental procedure, refer to Ref. [74].

The variation of the slope k_v of the regression line relating V_f and $\mu_{r,mean}$ with the element thickness h_U is shown in Fig. 17. The results can be normalized by the slope of the line for any chosen reference thickness, $h_{U,ref}$, used in the calibration process. It becomes apparent that the measurements are no longer affected for thicknesses beyond $h_U = 70$ mm. Whenever the thickness of the element under analysis does not match the thickness of the specimens used in the laboratory to fit the regression line, k_v should be corrected using the following equation:

$$\frac{k_v}{k_{v,ref}} = \sqrt{\frac{1 - e^{-0.0642 h_U}}{1 - e^{-0.0642 h_{U,ref}}}} \tag{13}$$

where k_v and $k_{v,ref}$ are the slopes of the regression lines obtained in specimens with the thickness h_U and $h_{U,ref}$, respectively, expressed in milimeters.

5.2. Area surrounding the probe

The experiments described in Ref. [74] show that the $\mu_{r,mean}$, and so the V_f estimates are affected by the variation of the area surrounding the

Fig. 16. Fibre anisometry: Eq. (12) vs experimental data.
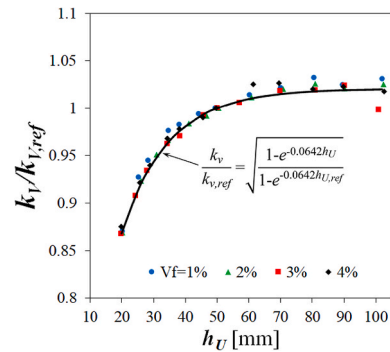
Fig. 17. Dependence of k_V with thickness of the element considering $h_{U,ref} = 50$ mm.

measuring point. This effect disappears when the probe is centered at no less than 100 mm from the nearest edge and can be considered negligible (with an error around 2 %) when the distance to the nearest edge is 75 mm.

5.3. Segregation of the fibres

As the inductance measurements are performed on one face of the UHPFRC element, it is expected that if the fibres are not evenly distributed across the thickness and more concentrated towards one the of the surfaces, the $\mu_{r,mean}$, and so the V_f estimates, may be affected. To analyse this effect, 12 plates with dimensions $200 \times 200 \times 30$ mm^3 and fibre content of 1 %, 2 %, 3 % and 4 % were cast. The mix is identical to that used in the previous sections. The groups of plates are considered: HOk – Horizontal cast with fibres oriented with external magnetic field; HRk – Horizontal cast without forced orientation of the fibres; and VRk- – Vertically cast without forced orientation of the fibres. The index k refers to the fibre content (1, 2, 3 and 4 %). It is worth pointing that the x-axis in HOk plates refers to preferential orientation of the fibres, whereas in VRk refers to the vertical casting direction.

The NDT measurements were performed at the centre of the moulded surfaces (bottom surface in the case of the HOk and HRk specimens). Afterwards, $30 \times 30 \times 30$ mm^3 cubes were extracted for determining the number of fibres (N_f) intersecting a cross-section normal to x- or y-axis through image analysis. The variation of the number of fibres through the thickness of the elements is shown in Fig. 18. The results. Show that the HR$_k$ specimens exhibit fibre segregation towards the bottom surface. As shown in Fig. 19, this affects directly the slope of the regression line relating V_f and $\mu_{r,mean}$, with a larger k_v value being necessary to fit the results from the HRk series. It is interesting to confirm that the data points corresponding to specimens HOk and VRk are fitted by the same line, irrespective of the way they were cast.

(c)

5.4. Surface finishing

Poor contact between the probe and the UHPFRC surface introduces leakage of the magnetic flux and affects the inductance measurements. The best measuring conditions are always obtained over moulded surfaces, which have smooth finishing. The opposite occurs over rough casting surfaces. A remedial measure is to smooth the surface before performing the inductance measurements, as depicted in Fig. 20 (a).

The plates of the series HOk mentioned in the previous section were selected for evaluation of this effect. As shown in Fig. 19, these plates did not show fibre segregation, with $\mu_{r,mean}$ values measured over the moulded surface identical to those of the vertically cast plates. The
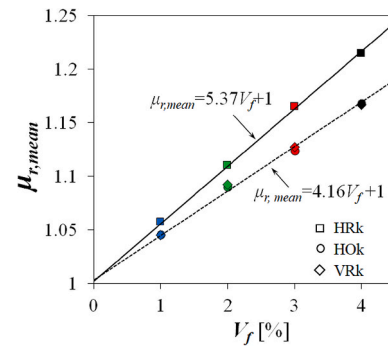

Fig. 19. Effect of the segregation on the relation between V_f and $\mu_{r,mean}$. Segregation towards the bottom surface over which the measurements were taken was observed in specimens HRk.

specimens are now labelled according to the type of surface where the measurements where performed: C – casting, natural finishing, S – casting, smoothed finishing and M – moulded. It becomes apparent that the smoothing improves the contact between the probe and the UHPFRC surface, but it was not enough to achieve the same $\mu_{r,mean}$ values as in the moulded surface. Therefore, the calibration of the regression to be used in the measurements in a real structure must be made on a similar type of surface.

6. Estimation of the tensile strength

The proposed NDT method is immediately applicable for quality control of thin UHPFRC elements in the sense that provides a simple way to measure the local fibre content, V_f, as well as the fibre orientation factor, $\alpha_{0,i}$, along any direction of interest. In the following, it is shown how the NDT measurements can also be used to determine the post cracking tensile strength $f_{Utu,i}$.

6.1. Validation on small specimens

In previous works the validity of Eq. (1) was assessed performing direct tensile tests (UTT) [13,17] and double-edge wedge splitting tests (DEWST1) [20] to determine f_{Utu}, accompanied by image analysis to determine $\alpha_{0,i}$ (Eq. B. (1)) and $\alpha_{1,i}$ (Eq. B. (7)), and so the fibre structure parameter, λ_{IA}. As shown in Fig. 21 (a), this allowed estimating the representative fibre-to-matrix bond strength, $\tau_f = 11.1$ MPa, for the UHPFRC mix used in this work.

According to the procedures described elsewhere [30–32],

(a)

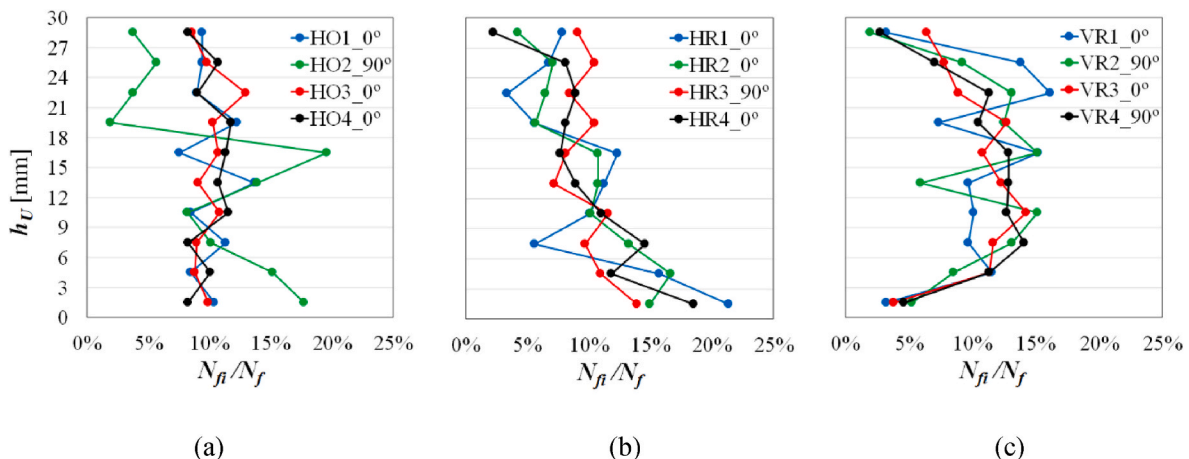(b)

(c)

Fig. 18. Distribution of the fibres through the thickness: (a) HOk series; (b) HRk series; (c) VRk series.
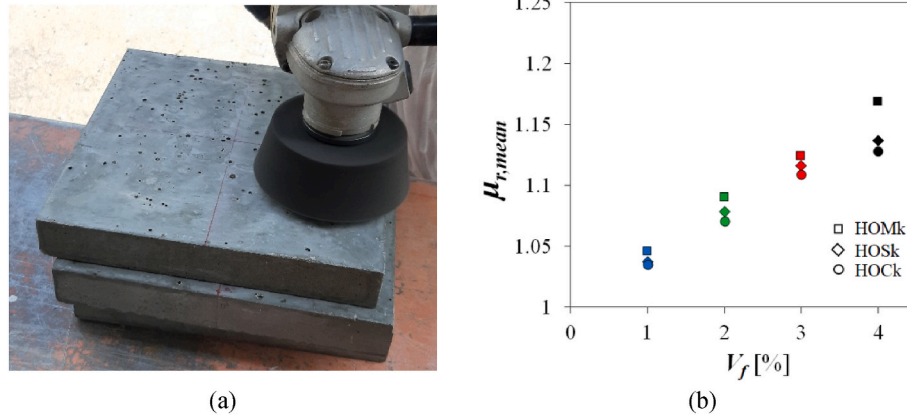
Fig. 20. Surface effect on $\mu_{r,mean}$: (a) mechanical smoothing of the casting surface; (b) regression lines for the different surface types.
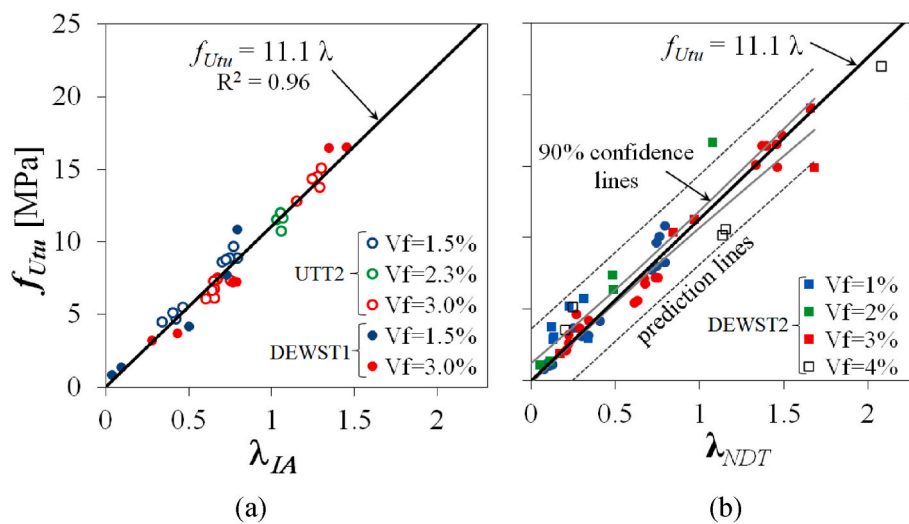

Fig. 21. Relations between f_{Utu} and λ from (a) image analysis [13] and (b) NDT method.

additional double-edge wedge splitting tests on the specimens designated in Table 1 as DEWST2 were carried out. Instead of using image analysis, the NDT measurements were used to determine the fibre structure parameter λ_{NDT}: Fig. 21(b) shows the results obtained for the test series DEWST1 and DEWST2, together with the 90 % confidence band for the regression. The corresponding tabular data is provided in Appendix Eof the supplementary material. Compared to Fig. 21(a) the scatter has increased, with some data points lying outside the 90 % prediction band, but it is noteworthy the fact that the line $f_{Utu} = 11.1\lambda$ is within the 90 % confidence band of the regression, which further confirms the applicability of the NDT method. The data points corresponding to specimens with $V_f = 4$ % were excluded from the regression. These points are systematically bellow the regression line, which may indicate that the validity of the linear model $f_{Utu} = \tau_f \lambda$ for such high fibre contents becomes questionable. This is expected since signs of fibre agglomeration were observed for these specimens.

6.2. Tensile strength prediction of a thin UHPFRC plate

6.2.1. Non-destructive measurements

A thin plate of $900 \times 1100 \times 30$ mm^3 was cast horizontally using mixture with 3 % vol. Of fibres. The mix is that characterized in Refs. [13,17,20], the same as in the UTT and DEWST1 specimens in Fig. 21 and in the experiments described in section 5. The fresh mixture was poured in the point (CP: $x = 400$, $y = 500$ mm) and then vibrated on a vibrating table to help the material fill the mould, see Fig. 22.

The NDT measurements were performed over an area of 700×900 mm^2 (respecting a 100 mm clearance from each border to avoid the boundary effects). The measuring grid of 50×50 mm^2 contained $15 \times 19 = 285$ points. Three non-collinear measurements were made on each point, and always on the moulded (bottom) surface.

The directions of preferential fibre orientation were determined through the usual tensor operations and are represented by ellipses in Fig. 23(a). The major and minor radius are proportional to the
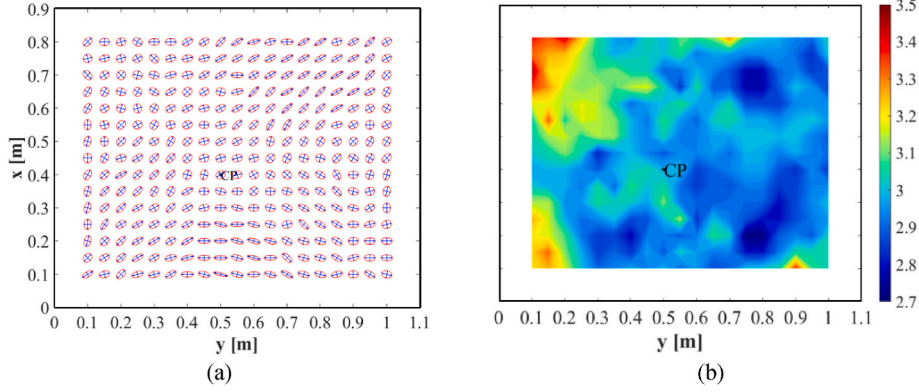

Fig. 22. Casting the plate.

Fig. 23. NDT results: (a) fibre anisometry and (b) contour maps with the vibre volumetric fraction [%].

corresponding fibre orientation factors. These were determined using Eq. (11) with $k_\alpha = 1.84$ and $\alpha_0 = 0.54$ as resulting from Table C1 considering the ratio $h_U/l_f = 2.5$. The fibres tend to be preferentially oriented from the CP towards the bottom-left and top-right corners. Among all points and directions, the maximum orientation factor $\alpha_{0,i}$ reached 0.88 and the minimum 0.19. The average values along x and y-directions equal 0.48 and 0.6, respectively.

The fibre content was determined using $k_v = 4.1$ in Eq. (9). The colour map with the variation of V_f throughout the plate is shown in Fig. 23(b). The overall dispersion is 0.12 % with the range from 2.76 to 3.47 %. The global average is 3 %, confirming the adequacy of the adopted k_v value.

The post-cracking tensile strengths in x-direction, $f_{Utu,x}$ and y-direction, $f_{Utu,y}$, were estimated applying the regression line of Fig. 21(a), with λ_i determined based on the known geometry of the fibres ($l_f/d_f = 60$), V_f and $\alpha_{0,i}$ determined from NDT and $\alpha_{1,i}$ from Eq. B. (7). The contour maps are presented in Fig. 24 and a large variability can be seen with values in the range 3–15 MPa. It is remarked that the 2nd order tensor approximation allows the determination $f_{Utu,i}$ not only in the x and y-directions, but along any direction of interest.

6.2.2. Four-point bending test

After the NDT measurements, the plate was cut to obtain 10 specimens with approximately $100 \times 600 \times 30$ mm^3 to be tested under four-point bending according to the French norm NF P18-470 [28] recommendations for thin elements. The location, orientation and numbering of the specimens is marked in Fig. 24. The region of constant bending moment is delimited by the dashed lines. The tests were conducted under vertical displacement control with a rate of 0.25 mm/min. Two LVDTs were placed at mid-span to measure displacements, according to the setup depicted in Fig. 25 (a).

The locations of the critical cracks were the deformation localized are marked in Fig. 24. In most cases it is evident that the cracks formed within, or close to, the segment with maximum moment, but following the regions identified by the NDT method as having lower values of $f_{Utu,i}$. The clear exception is specimen #8. However, it should be noted that due to the viscosity of the material, the casting surface was somewhat irregular, and crack localization may have be affected by the surface irregularities. The average thickness of each of the specimens is indicated in Table 2. It is notable that in the case of specimens 4 and 5 the shape of the cracks clearly suggests that they formed following the path of least resistance.

The bending moment versus the average midspan displacement curves are plotted in Fig. 25. As expected from the NDT results, the variability is significant. A simplified inverse analysis following the procedures indicated in the French norm [28] was developed to derive the simplified elastic-plastic UHPFRC constitutive law up to the onset of strain localization The outcomes of the analysis are f_{Utu} and the strain at onset of crack localization, ε_{Utu}. The elasticity modulus $E_U = 42$ GPa was determined using the average slope at the origin of the M-δ curves of Fig. 25, taking into account the real average thickness, h_U, of each specimen.

The results from the simplified back analysis and the post-cracking tensile strength estimate from the NDT method are presented in Table 2. The latter refers to the average values determined from the NDT measurements over the crack cross-section, and along the respective direction, i.e., $f_{Utu,x}$ NDT for specimens 1, 2 and 3, and $f_{Utu,y}$ NDT, otherwise. The agreement is noticeable, with the exception of specimens 8 and 9. The average ratio $f_{Utu,i}$ NDT$/f_{Utu}$ FPBT $= 1.08$, with a standard deviation of 0.11. This results indicate that the proposed procedure for estimation of the residual tensile strength of the UHPFRC in thin elements provides a feasible alternative to mechanical testing.
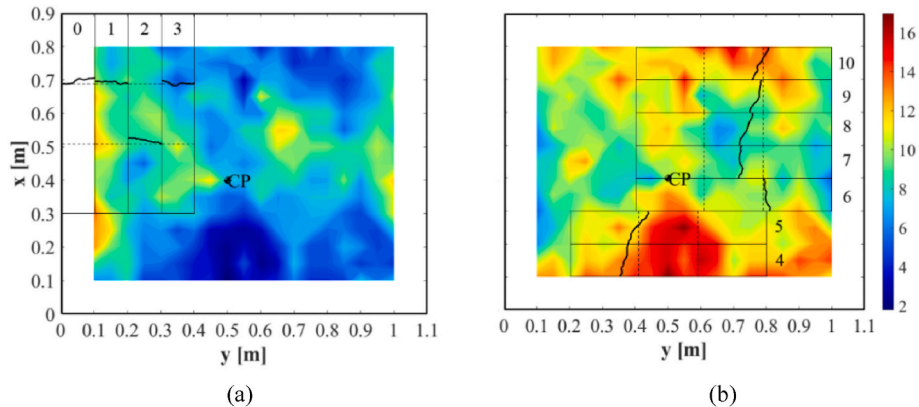

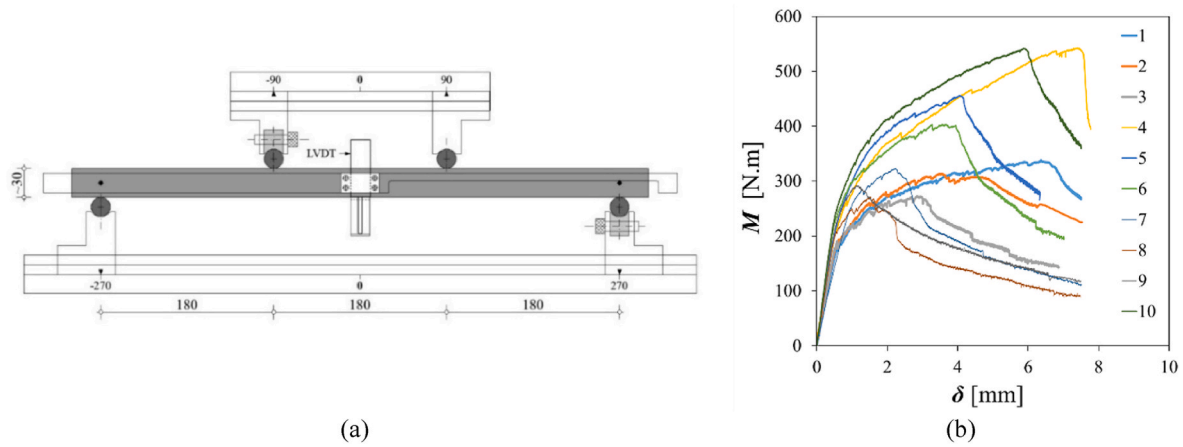**Fig. 24.** NDT tensile strength [MPa] contour maps and FPBT cracks of LP1 (a) $f_{Utu,x}$ and (b) $f_{Utu,y}$.

Fig. 25. Four-point bending test: (a) scheme of the test setup: (b) results for specimens 1 to 10.

Table 2
Comparison between results from simplified back analysis of FPBT and NDT method.

Specimen	h_U	$\alpha_{0,i}^{NDT}$	M	δ	χ	ε_{Utu}	f_{Utu}^{FPBT}	$f_{Utu,i}^{NDT}$	$f_{Utu,i}^{NDT}/f_{Utu}^{FPBT}$
	[mm]		[N.m]	[mm]	[m^{-1}]	[‰]	[MPa]	[MPa]	
1	30.2	0.51	338	6.36	0.205	4.30	9.49	9.33	0.98
2	30.3	0.54	313	3.55	0.114	2.03	9.09	8.91	0.98
3	31.4	0.50	272	2.84	0.091	1.66	7.72	8.38	1.09
4	32.2	0.67	542	7.40	0.238	5.15	13.35	12.58	0.94
5	32.7	0.63	456	4.04	0.130	2.49	11.18	11.32	1.01
6	34.1	0.59	403	3.56	0.115	2.34	9.64	10.32	1.07
7	33.8	0.54	323	2.24	0.072	1.29	7.92	9.00	1.14
8	33.7	0.54	271	1.52	0.049	0.74	7.05	8.94	1.27
9	34.3	0.60	291	1.14	0.037	0.38	7.98	10.13	1.27
10	33.9	0.67	542	5.87	0.189	4.18	12.19	12.73	1.04
Min.	30.2	0.50	271	1.14	0.037	0.38	7.05	8.38	0.94
Max.	34.3	0.67	542	7.40	0.238	5.15	13.35	12.73	1.27
Average									1.08
Standard deviation									0.11

h_U - Average thickness measured for each specimen.
$\alpha_{0,i}^{NDT}$ – fibre orientation factor determined using NDT at the cross section where the critical crack formed.
M – midspan flexural moment corresponding to the peak load obtained in the experiment.
δ – midspan deflection at peak load measured in the experiment.
χ – cross-section curvature at peak load determined through inverse analysis according to NF P18-470.
ε_{Utu} – Strain at the onset of localization determined through inverse analysis according to NF P18-470.
f_{Utu}^{FPBT} – Post cracking tensile strength determined through inverse analysis according to NF P18-470.
f_{Utu}^{NDT} – Post cracking tensile strength calculated using Eq. (1), the NDT measurements to determine V_f, $\alpha_{0,i}$ and $\alpha_{1,i}$, and t_f = 11.1 MPa as shown in section 6.1.

7. Conclusions

This work presents further developments on the NDT magnetic method proposed in Refs. [20,65] for quality control of thin UHPFRC elements containing short steel fibres, whenever they can be assumed to be predominantly oriented along the in-plane directions. The method allows determining the fibre content and the fibre orientation factor, which can be used to estimate the directionally dependent post-cracking tensile strength of the material as placed in the structure.

The model for the determining relative magnetic permeability of the composite was generalized to accommodate any probability density function describing the fibre orientation. Introducing in the equations the probability density function described in section 3, we could prove that.

- the relation between the volumetric fibre fraction (V_f) and the average relative magnetic permability along any two orthogonal drections ($\mu_{r,mean}$) is nearly linear, irrespective of the fibre orientation distribution. This confirms the previous and the new experimental data;

- for the range fibre orientation distributions that can be expected in practice, the relation between α_0 and ρ_{xy} is well approximated by a linear equation and is practically independent of the fibre content. Again, this is confirmed by the previous and by new experimental data and provides fundamental theoretical support to the method, which was not yet available;

- the relative magnetic permeability can be represented by a second order tensor. This allows determining the scalar fibre orientation indicators, and consequently the post-cracking tensile strength (f_{Utu}), along any direction of interest based on any there non-collinear magnetic inductance measurements;

- in particular, the development above allows plotting the directions of maximum and minimum fibre orientation in each measuring point.

The influence on the relative magnetic permeability estimates of factors that cannot be described by the model of the magnetic circuit, such as the element thickness, surface finishing, the fibre sedimentation across the thickness and the distance of the probe to the boundaries were summarized. It was shown that the magnetic probe used in this study is capable of evaluating the fibre content and fibre orientation in the UHPFRC up to a depth of 70 mm measured from the contact surface and

that the measurements should be taken at least 75 mm away from the nearest border. An equation was proposed to correct the slope of the line relating V_f and $\mu_{r,mean}$ to account for the effect thickness of the element. The measurement should be taken preferably on moulded surfaces. In case this is not possible, the surface unevenness should be smoothed. The magnetic measurements are highly sensitive to fibre settlement across the thickness, due to excessive agitation during casting or excessive fluidity of the material in the fresh state.

A methodology is proposed for using the NDT method for estimating the post-cracking tensile strength of the UHFRC in thin elements in which the fibres are predominantly orientated along the in-plane directions. The procedure was validated in a $900 \times 1100 \times 30$ mm^3 plate. In case a previous laboratory characterization of the material is available providing the representative value of the fibre-to-matrix bond strength (τ_f), the NDT method allows estimating the UHPFRC tensile strength with similar accuracy to that obtained by testing samples extracted from the structure. It is concluded that the NDT method used here can be a turning point in the quality control procedures adopted in real applications.

CRediT authorship contribution statement

Mário Pimentel: Writing – review & editing, Writing – original draft, Validation, Supervision, Resources, Project administration, Methodology, Funding acquisition, Conceptualization. **Aurélio Sine:** Writing – original draft, Methodology, Investigation, Formal analysis, Data curation, Conceptualization. **Sandra Nunes:** Writing – review & editing, Validation, Supervision, Resources, Methodology, Conceptualization.

Declaration of competing interest

The authors declare that they have no known competing financial interests or personal relationships that could have appeared to influence the work reported in this paper.

Data availability

Data will be made available on request.

Acknowledgements

Appendix A. Supplementary data

Supplementary data to this article can be found online at https://doi.org/10.1016/j.ndteint.2024.103128.

References

[1] Richard P, Cheyrezy M. Composition of reactive powder concretes. Cement Concr Res 1995;25(7):1501–11.

[2] Naaman AE, Wille K. The path to ultra-high performance fiber reinforced concrete (UHP-frc): five decades of progress. In: Proceedings of HiperMat 2012; 2012. p. 3–15.

[3] Haber ZB, De La Varga I, Graybeal BA. Properties and behavior of UHPC-class materials. Georgetown pike: U.S. Department of transportation. Federal Highway Administration; 2018.

[4] Habel K, Denarié E, Brühwiler E. Structural response of elements combining and reinforced concrete. J Struct Eng 2006;132(November):1793–800. https://doi.org/10.1061/?ASCE?0733-9445?2006?132:11?1793?.

[5] Brühwiler E, Denarié E. Rehabilitation and strengthening of concrete structures using ultra-high performance fibre reinforced concrete. Struct Eng Int 2013;23(4):450–7. https://doi.org/10.2749/101686613X13627347100437.

[6] Denarié E, Jacomo D, Fady N, Corvez D. Rejuvenation of maritime signalisation structures with UHPFRC. In: RILEM-fib-AFGC int. Symposium on ultra-high performance fibre-reinforced concrete; 2013. p. 1–10.

[7] Mirkhalaf SM, Eggels EH, van Beurden TJH, Larsson F, Fagerström M. A finite element based orientation averaging method for predicting elastic properties of short fiber reinforced composites. Composites Part B Dec. 2020;202. https://doi.org/10.1016/J.COMPOSITESB.2020.108388.

[8] Mortazavian S, Fatemi A. Effects of fiber orientation and anisotropy on tensile strength and elastic modulus of short fiber reinforced polymer composites. Composites Part B Apr. 2015;72:116–29. https://doi.org/10.1016/J.COMPOSITESB.2014.11.041.

[9] Lee D. Local anisotropy analysis based on the Mori-Tanaka model for multiphase composites with fiber length and orientation distributions. Composites Part B Sep. 2018;148:227–34. https://doi.org/10.1016/J.COMPOSITESB.2018.04.050.

[10] Zhan Jian, Denarié Emmanuel, Brühwiler Eugen. Elastic limit tensile stress of UHPFRC: method of determination and effect of fiber orientation. Cement Concr Compos 2023;140:105122. https://doi.org/10.1016/j.cemconcomp.2023.105122.

[11] Kang ST, Kim JK. The relation between fiber orientation and tensile behavior in an ultra high performance fiber reinforced cementitious composites (UHPFRCC). Cement Concr Res 2011;41(10):1001–14. https://doi.org/10.1016/j.cemconres.2011.05.009.

[12] Bastien-Masse M, Denarié E, Brühwiler E. Effect of fiber orientation on the in-plane tensile response of UHPFRC reinforcement layers. Cem Concr Compos 2016:111–25. https://doi.org/10.1016/j.cemconcomp.2016.01.001.

[13] Abrishambaf A, Pimentel M, Nunes S. Influence of fibre orientation on the tensile behaviour of ultra-high performance fibre reinforced cementitious composites. Cement Concr Res 2017:28–40. https://doi.org/10.1016/j.cemconres.2017.03.007.

[14] Duque LFM, Graybeal B. Fiber orientation distribution and tensile mechanical response in UHPFRC. Mater. Struct. Constr. 2017;50(1). https://doi.org/10.1617/s11527-016-0914-5.

[15] Chun B, Yoo DY. Hybrid effect of macro and micro steel fibers on the pullout and tensile behaviors of ultra-high-performance concrete. Composites Part B Apr. 2019;162:344–60. https://doi.org/10.1016/J.COMPOSITESB.2018.11.026.

[16] Wuest J. Comportement structural des bétons de fibres ultra performants en traction dans des éléments composés. EPFL Thesis 3987. École Polytechnique Fédérale de Lausanne 2007. https://doi.org/10.5075/epfl-thesis-3987.

[17] Abrishambaf A, Pimentel M, Nunes S. A meso-mechanical model to simulate the tensile behaviour of ultra-high performance fibre-reinforced cementitious composites. Compos Struct 2019;222. https://doi.org/10.1016/j.compstruct.2019.110911.

[18] Naaman AE. A statistical theory of strength for fiber reinforced concrete. Massachusetts Institute of Technology; 1972.

[19] Naaman AE. High performance fiber reinforced composites. In: Shi C, Mo YL, editors. High-performance construction materials: science and applications. World Scientific Publishing Co. Pte. Ltd.; 2008. p. 91–153.

[20] Nunes S, Pimentel M, Ribeiro F, Milheiro-Oliveira P, Carvalho A. Estimation of the tensile strength of UHPFRC layers based on non-destructive assessment of the fibre content and orientation. Cem Concr Compos 2017;83:222–38. https://doi.org/10.1016/j.cemconcomp.2017.07.019.

[21] Pyo S, El-Tawil S, Naaman AE. Direct tensile behavior of ultra high performance fiber reinforced concrete (UHP-FRC) at high strain rates. Cement Concr Res 2016;88:144–56. https://doi.org/10.1016/j.cemconres.2016.07.003.

[22] Graybeal BA, Baby F. Development of direct tension test method for ultra-high-performance fiber-reinforced concrete. ACI Mater J 2013;(110):177–86. https://doi.org/10.14359/51685532.

[23] Qian S, Li VC. Simplified inverse method for determining the tensile strain capacity of strain hardening cementitious composites. J Adv Concr Technol 2007;5(2):235–46.

[24] Baby F, Graybeal B, Marchand P, Toutlemonde F. Proposed flexural test method and associated inverse analysis for ultra-high-performance fiber-reinforced concrete. ACI Mater J 2012;109(5):545–55.

[25] Baby F, Graybeal BA, Marchand P, Toutlemonde F. UHPFRC tensile behavior characterization: inverse analysis of four-point bending test results. Mater Struct 2013;46(8):1337–54. https://doi.org/10.1617/s11527-012-9977-0.

[26] López JÁ, Serna P, Navarro-Gregori J, Camacho E. An inverse analysis method based on deflection to curvature transformation to determine the tensile properties of UHPFRC. Mater Struct 2015;48(11):3703–18. https://doi.org/10.1617/s11527-014-0434-0.

[27] AFGC, *Bétons fibrés à ultra-hautes performances (Ultra high performance fibrereinforced concretes)-Recommandations.* France; 2013.

[28] Afnor Norme PR. NF P18-470|Bétons fibrés à Ultra Hautes Performances Spécification, performance. production et conformité. France; 2016. p. 1–79.

[29] López JÁ, Serna P, Navarro-Gregori J, Coll H. A simplified five-point inverse analysis method to determine the tensile properties of UHPFRC from unnotched four-point bending tests. Composites Part B Apr. 2016;91:189–204. https://doi.org/10.1016/J.COMPOSITESB.2016.01.026.

[30] di Prisco M, Ferrara L, Lamperti MGL. Double-edge wedge splitting test: preliminary results. Fract. Mech. Concr. Concr. Struct. 2010:1579–86.

[31] di Prisco M, Ferrara L, Lamperti MGL. Double edge wedge splitting (DEWS): an indirect tension test to identify post-cracking behaviour of fibre reinforced cementitious composites. Mater Struct 2013;46(11):1893–918. https://doi.org/10.1617/s11527-013-0028-2.

[32] Pimentel M, Nunes S. On the double-edge wedge-splitting test for the characterisation of HPFRC in uniaxial tension. In: Proceedings of 4th international symposium on ultra-high performance concrete and high performance materials (HiPerMat); 2016.

[33] Babut R. Structural investigation of steel fibre reinforced concrete. Heron 1985;31(2):29–43.

[34] Stähli P, van Mier JGM. Manufacturing, fibre anisotropy and fracture of hybrid fibre concrete. Eng Fract Mech 2007;74(1–2):223–42. https://doi.org/10.1016/J.ENGFRACMECH.2006.01.028.

[35] Zhou B, Uchida Y. Influence of flowability, casting time and formwork geometry on fiber orientation and mechanical properties of UHPFRC. Cement Concr Res 2017;95:164–77. https://doi.org/10.1016/j.cemconres.2017.02.017.

[36] Stähli P, Custer R, van Mier JGM. On flow properties, fibre distribution, fibre orientation and flexural behaviour of FRC. Mater Struct 2008;41(1):189–96. https://doi.org/10.1617/s11527-007-9229-x.

[37] Ferrara L, Meda A. Relationships between fibre distribution, workability and the mechanical properties of SFRC applied to precast roof elements. Mater Struct 2007;39(4):411–20. https://doi.org/10.1617/s11527-005-9017-4.

[38] Abrishambaf A, Barros JAO, Cunha VMCF. Relation between fibre distribution and post-cracking behaviour in steel fibre reinforced self-compacting concrete panels. Cement Concr Res 2013;51:57–66. https://doi.org/10.1016/J.CEMCONRES.2013.04.009.

[39] Laranjeira F, Aguado A, Molins C, Grünewald S, Walraven J, Cavalaro S. Framework to predict the orientation of fibers in FRC: a novel philosophy. Cement Concr Res 2012;42(6):752–68. https://doi.org/10.1016/j.cemconres.2012.02.013.

[40] Ferrara L, Ozyurt N, di Prisco M. High mechanical performance of fibre reinforced cementitious composites: the role of 'casting-flow induced' fibre orientation. Mater Struct 2011;44(1):109–28. https://doi.org/10.1617/s11527-010-9613-9.

[41] Martinie L, Roussel N. Simple tools for fiber orientation prediction in industrial practice. Cement Concr Res 2011;41(10):993–1000. https://doi.org/10.1016/J.CEMCONRES.2011.05.008.

[42] Deeb R, Karihaloo BL, Kulasegaram S. Reorientation of short steel fibres during the flow of self-compacting concrete mix and determination of the fibre orientation factor. Cement Concr Res Feb. 2014;56:112–20. https://doi.org/10.1016/J.CEMCONRES.2013.10.002.

[43] Stroeven P, Hu J. Effectiveness near boundaries of fibre reinforcement in concrete. Mater Struct 2006;39:1001–13. https://doi.org/10.1617/s11527-006-9101-4.

[44] Stroeven P. Stereology of concrete reinforced with short steel fibres. Heron 1986;31(2).

[45] Nemati KM, Stroeven P. Stereological analysis of micromechanical behavior of concrete. 2001.

[46] Stroeven P. Stereological principles of spatial modeling applied to steel fiber-reinforced concrete in tension 2009;106(3):213–22.

[47] Aveston J, Kelly A. Theory of multiple fracture of fibrous composites. J Mater Sci Mar. 1973;8(3):352–62. https://doi.org/10.1007/BF00550155.

[48] Alberti MG, Enfedaque A, Gálvez JC. A review on the assessment and prediction of the orientation and distribution of fibres for concrete. Composites Part B 2018;151 (March):274–90. https://doi.org/10.1016/j.compositesb.2018.05.040.

[49] Pimentel M, Nunes S. Determination of the tensile response of UHPFRC layers using a non-destructive method for assessing the fiber content and orientation. In: Proceedings of the 9th international conference on fracture mechanics of concrete and concrete structures; 2016.

[50] Nunes S, Pimentel M, Carvalho A. Non-destructive assessment of fibre content and orientation in UHPFRC reinforcement layers. In: Proceedings of 4th international symposium on ultra-high performance concrete and high performance materials (HiPerMat); 2016.

[51] Ferrara L, et al. Structural elements made with highly flowable UHPFRC: correlating computational fluid dynamics (CFD) predictions and non-destructive survey of fiber dispersion with failure modes. Eng Struct 2017;133:151–71. https://doi.org/10.1016/J.ENGSTRUCT.2016.12.026.

[52] Zhou B, Uchida Y. Relationship between fiber orientation/distribution and post-cracking behaviour in ultra-high-performance fiber-reinforced concrete (UHPFRC). Cem Concr Compos 2017;83:66–75. https://doi.org/10.1016/j.cemconcomp.2017.07.007.

[53] Oesterlee C. Structural response of reinforced UHPFRC and RC composite members. École Polytechnique Fédérale de Lausanne; 2010.

[54] Shen X, Brühwiler E. Influence of local fiber distribution on tensile behavior of strain hardening UHPFRC using NDT and DIC. Cement Concr Res 2020;132. https://doi.org/10.1016/j.cemconres.2020.106042.

[55] Lataste JF, Behloul M, Breysse D. Characterisation of fibres distribution in a steel fibre reinforced concrete with electrical resistivity measurements. NDT E Int 2008;41(8):638–47. https://doi.org/10.1016/j.ndteint.2008.03.008.

[56] Sirieix C, Lataste JF, Breysse D, Naar S, Dérobert X. Comparison of nondestructive testing: infrared thermography, electrical resisitivity and capacity methods for assessing a reinforced concrete structure. J Build Apprais 2007;3(1):77–88. https://doi.org/10.1057/palgrave.jba.2950065.

[57] Barnett SJ, Lataste JF, Parry T, Millard SG, Soutsos MN. Assessment of fibre orientation in ultra high performance fibre reinforced concrete and its effect on flexural strength. Mater. Struct. Constr. 2010;43(7):1009–23. https://doi.org/10.1617/s11527-009-9562-3.

[58] Martinie L, Lataste JF, Roussel N. Fiber orientation during casting of UHPFRC: electrical resistivity measurements, image analysis and numerical simulations. Mater. Struct. Constr. 2015;48(4):947–57. https://doi.org/10.1617/s11527-013-0205-3.

[59] Woo LY, Wansom S, Ozyurt N, Mu B, Shah SP, Mason TO. Characterizing fiber dispersion in cement composites using AC-Impedance Spectroscopy. Cem Concr Compos 2005;27(6):627–36. https://doi.org/10.1016/j.cemconcomp.2004.06.003.

[60] Ferrara L, Faifer M, Toscani S. A magnetic method for non destructive monitoring of fiber dispersion and orientation in steel fiber reinforced cementitious composites—part 1: method calibration. Mater Struct 2012;45(4):575–89. https://doi.org/10.1617/s11527-011-9793-y.

[61] Ferrara L, Faifer M, Milot M, Toscani S. A magnetic method for non destructive monitoring of fiber dispersion and orientation in steel fiber reinforced cementitious composites. Part 2: correlation to tensile fracture toughness. Mater Struct 2012;45:591–8. https://doi.org/10.1617/s11527-011-9794-x.

[62] Faifer M, Ferrara L, Ottoboni R, Toscani S. Low frequency electrical and magnetic methods for non-destructive analysis of fiber dispersion in fiber reinforced cementitious composites: an overview. Sensors 2013;13(1):1300–18. https://doi.org/10.3390/s130101300.

[63] Torrents JM, Blanco A, Pujadas P, Aguado A, Juan-García P, Sánchez-Moragues MÁ. Inductive method for assessing the amount and orientation of steel fibers in concrete. Mater Struct 2012;45(10):1577–92. https://doi.org/10.1617/s11527-012-9858-6.

[64] Cavalaro SHP, López-Carreño R, Torrents JM, Aguado A, Juan-García P. Assessment of fibre content and 3D profile in cylindrical SFRC specimens. Mater. Struct. Constr. 2016;49(1–2):577–95. https://doi.org/10.1617/s11527-014-0521-2.

[65] Nunes S, Pimentel M, Carvalho A. Non-destructive assessment of fibre content and orientation in UHPFRC layers based on a magnetic method. Cem Concr Compos 2016;72:66–79. https://doi.org/10.1016/j.cemconcomp.2016.05.024.

[66] Li L, Xia J, Chin C, Jones S. Fibre distribution characterization of ultra-high performance fibre-reinforced concrete (Uhpfrc) plates using magnetic probes. Materials 2020;13(22):1–20. https://doi.org/10.3390/ma13225064.

[67] Sawicki B, Brühwiler E, Denarié E. Inverse analysis of R-UHPFRC beams to determine the flexural response under service loading and at ultimate resistance. ASCE Journal of Structural Engineering 2022;148(2):04021260.

[68] SIA, prSIA2052:2023-02 - Béton fibré ultra-performant (BFUP) – Matériaux, dimensionnement et exécution. Société suisse des ingénieurs et des architectes, Zurich..

[69] Lu C, Leung CKY. Theoretical evaluation of fiber orientation and its effects on mechanical properties in Engineered Cementitious Composites (ECC) with various thicknesses. Cement Concr Res 2017;95:240–6. https://doi.org/10.1016/j.cemconres.2017.02.024.

[70] Dupont D, Vandewalle L. Distribution of steel fibres in rectangular sections. Cem Concr Compos 2005;27(3):391–8. https://doi.org/10.1016/j.cemconcomp.2004.03.005.

[71] AFNOR. NF P 18-710: national addition to Eurocode 2 - design of concrete structures: specific rules for UHPFRC. France; 2016.

[72] Advani SG, Tucker CL. The use of tensors to describe and predict fiber orientation in short fiber composites. J Rheol 1987;31(8):751–84. https://doi.org/10.1122/1.549945.

[73] Guenet T. Modélisation du comportement des bétons fibrés à ultra-hautes performances par la micromécanique : effet de l'orientation des fibres à l'échelle de la structure. Université Paris-Est; 2016.

[74] Nunes S, Pimentel M, Sine A, Mokhberdoran P. Key factors for implementing magnetic NDT method on thin UHPFRC bridge elements. Materials 2021;14:4353. https://doi.org/10.3390/ma14164353.